Research Article
Open Access

MJ Cell Press

MJ Engineering Sciences

Available at: https://mjcellpress.com/article/mjes05/

MJ Engineering Sciences

The Use of Aster data for carbonate and silicate minerals exploration in the North region of Cameroon using Spectral Angle Mapper

Kamta Touoyem Guy Olivier[1*], Jacques Matanga[1], Kabiena Ivan Basile[1], Maka Maka Ebenezer[1], Malong Yannick[1], Ngounou Gamon Christian[2]

[1]Computer Engineering, Data Science and Artificial Intelligence Laboratory, National Polytechnic School of Douala, Cameroon

[2] Electrical engineering Department, National School of Technical Education, Cameroon

[*]Corresponding author: kamtaolivier@gmail.com

Key words

Aster data, Mineral exploration, Carbonates, silicates, Spectral Angle Mapper, North region of Cameroon.

Abstract

The identification and characterization of strategic mineral resources remain a critical challenge for developing countries such as Cameroon, where large portions of the territory are still insufficiently explored. This situation is particularly evident in the northern region, which hosts significant occurrences of carbonate minerals (e.g., calcite, dolomite) and silicate minerals (e.g., quartz, feldspars), both of which are of considerable importance for industrial applications.

This study evaluated the effectiveness of ASTER (Advanced Spaceborne Thermal Emission and Reflection Radiometer) satellite imagery in combination with the Spectral Angle Mapper (SAM) algorithm for detecting and mapping carbonate and silicate minerals in Northern Cameroon. The supervised SAM classifier was calibrated using spectral signatures from the ENVI 5.6 spectral library. The results confirmed that the method successfully identified and spatially delineated calcite, albite, and magnetite within the selected regions. These findings provide a valuable contribution to mineral exploration by improving knowledge of regional mineral distribution while simultaneously reducing the time and cost associated with conventional field-based surveys.

Received:11.01.2025 Accepted: 26.05.2025 Published online: 28.08.2025

How to cite this article: Kamta Touoyem G. O., J. Matanga., Kabiena I. B., Maka Maka E., Malong Y., & Ngounou Gamon C. (2025). *The Use of Aster data for carbonate and silicate minerals exploration in the North region of Cameroon using Spectral Angle Mapper*. *MJ Engineering Sciences*, *1*(1), 67–83. https://doi.org/10.63156/mjes05.

1. Introduction

The Republic of Cameroon, located in Central Africa, forms an integral part of the West African craton and presents a highly diverse geological environment, ranging from Precambrian basement rocks to recent sedimentary deposits. Despite this diversity, geological mapping and the overall knowledge of the country's mining potential remain limited and, in many cases, outdated. Furthermore, geophysical and geochemical data are either insufficient for large areas of the territory or require reinterpretation through more advanced analytical techniques.

Traditional mining exploration in Cameroon still relies heavily on field expeditions for data collection. However, the vast size of the country, its dense vegetation, and limited infrastructure pose significant challenges for geologists and prospectors. Field verification through geochemical sampling and laboratory testing often proves labor-intensive, time-consuming, and costly (Raunet, 2003). These constraints hinder the efficiency of conventional exploration methods and emphasize the need for alternative approaches, particularly in the northern part of the country (Figure 1).

Figure 1: Location of the North Region (in red) on the map of Cameroon

The use of satellite remote sensing, combined with artificial intelligence algorithms, offers promising solutions to these limitations. Hyperspectral remote sensing, in particular, has emerged over the past three decades as an effective tool for mineral exploration, enabling the detection and mapping of mineral deposits at regional and local scales (Zhang & Li, 2014). Today, remote sensing is considered indispensable in geological investigations, as it allows the identification of mineral signatures across vast and often inaccessible terrains.

In this context, ASTER (Advanced Spaceborne Thermal Emission and Reflection Radiometer) imagery represents a valuable resource for mineral exploration. It provides high-resolution multispectral data with spectral coverage well-suited for lithological studies (Ousmanou et al., 2024). Specifically, ASTER records reflected radiation in three bands of the visible-near infrared (VNIR, 0.52–0.86 µm) with a spatial resolution of 15 m, in six bands of the shortwave infrared (SWIR, 1.6–2.43 µm) with a resolution of 30 m, and in five bands of the thermal infrared (TIR, 8.125–11.65 µm) with a resolution of 90 m (Qi et al., 2018).

The identification of minerals using hyperspectral and multispectral imagery remains a complex task due to the intricate composition of minerals and the similarity of their spectral responses. Differentiating one mineral from another continues to be a challenge, as highlighted by Zeng et al. (2021). Nevertheless, the potential of these imaging technologies remains underexploited, particularly for mineral groups such as feldspars and calcites, which are of significant industrial importance. Feldspars play a central role in ceramics and glass manufacturing (Kyonka & Cook, 1954), while calcite ($CaCO_3$) is widely used in cement, paint, and other industries (Aquilano et

al., 2016). The exploitation of these resources could foster the development of local industries and support economic growth in northern Cameroon.

The presence of carbonate and silicate minerals is consistent with the geological context of the region, characterized by granitoid intrusions and feldspathic mineralization (Raunet, 2003). In this study, we aim to assess the effectiveness of ASTER satellite data combined with the Spectral Angle Mapper (SAM) algorithm for the identification and spatial mapping of carbonate and silicate minerals in the North Region of Cameroon.

2. Literature review

A wide variety of classification methods has been developed for hyperspectral image analysis, encompassing both supervised and unsupervised approaches (Plaza et al., 2009; Fauvel et al., 2012). Among these, supervised classification plays a central role, as it uses labeled training data to guide algorithms toward more accurate class discrimination.

Several studies, including those by Zhang and Li (2014) and Sudharsan et al. (2019a), have highlighted the importance of establishing strong correspondences between spectral libraries and the spectra of individual pixels. Within this framework, the Spectral Angle Mapper (SAM) has emerged as one of the most widely applied and reliable supervised classification techniques.

SAM measures the similarity between spectral vectors by calculating the spectral angle that separates them. In hyperspectral imagery, each pixel can be represented as an n-dimensional vector, where *n* corresponds to the number of spectral bands. The spectral angle between a given pixel and a reference spectrum from the library is then computed: the smaller the angle, the stronger the correspondence and the higher the similarity with the reference class (Kruse et al., 1993; Sudharsan et al., 2019a).

Compared with other supervised methods, such as the Maximum Likelihood Classifier (MLC) and Support Vector Machines (SVM), SAM offers the advantage of being relatively insensitive to illumination variations. This characteristic has made it particularly attractive for applications ranging from vegetation monitoring to mineral identification and urban mapping (Boardman, 1993; Li et al., 2012). Nevertheless, its performance decreases when discriminating between materials with very similar spectral signatures. To overcome this limitation, recent research has focused on hybrid approaches that combine SAM with statistical frameworks or deep learning models, thereby enhancing its overall classification performance (Yokoya et al., 2016).

The similarity between a target spectrum and a reference spectrum increases as the spectral angle decreases. The angle between a target spectrum vector **a** and a reference spectrum vector **b** is given by:

$$\alpha = \cos^{-1}\left(\frac{a \cdot b}{\|a\|\|b\|}\right) \qquad (1)$$

where ‖ - ‖ enotes the norm function. Equation (1) can also be expressed in expanded form as:

$$\alpha = \cos^{-1}\left[\frac{\sum_{i=1}^{n} a_i b_i}{[\sum_{i=1}^{n} a_i^2]^{\frac{1}{2}}[\sum_{i=1}^{n} b_i^2]^{\frac{1}{2}}}\right] \qquad (2)$$

The ASTER sensor is particularly attractive for geological remote sensing due to its large number of bands, relatively wide spectral range, and good spatial resolution. A key advantage of ASTER lies in its ability to detect emissions in the thermal infrared (TIR) spectrum, which extends beyond 2500 nm—exceeding the maximum wavelength of many modern hyperspectral sensors (Table 1). Moreover, ASTER's Band 3 in the visible-near infrared (VNIR) region provides additional benefits for lithological discrimination.

When compared with conventional multispectral sensors such as Landsat TM, ASTER offers notable improvements in spatial, spectral, and radiometric resolution, even though it is not a typical hyperspectral sensor.

These enhancements, together with improved data accessibility, have positioned ASTER as a critical dataset for geological mapping and mineral exploration (Rajendran & Nasir, 2017; Son et al., 2022; Islam et al., 2024).

Table 1: Spectral and spatial characteristics of the ASTER sensor compared with other multispectral and hyperspectral sensors.

ASTER			
Band	**Spectral Region**	**Wavelength (μm)**	**Resolution (m)**
Band 1	VNIR	0.52–0.60	15
Band 2		0.63–0.69	
Band 3		0.78–0.86	
Band 4		1.60–1.70	
Band 5	SWIR	2.145–2.185	30
Band 6		2.185–2.225	
Band 7		2.235–2.285	
Band 8		2.295–2.365	
Band 9		2.360–2.430	
Band 10	TIR	8.125–8.475	90
Band 11		8.475–8.825	
Band 12		8.925–9.275	
Band 13		10.25–10.95	
Band 14		10.95–11.65	

Research has also shown that carbonate and silicate minerals are well detected in the thermal infrared as shown in table 2 (Peyghambari & Zhang, 2021).

Table 2: mineral detection in different spectral bands

Group	**Mineral**	**Formula**	**Vnir (400-1000nm)**	**Swir (1000-25000nm)**	**Tir/Lwir (2500-14500)**	**Use**
OXIDES	Hematite	Fe2O3	Well Detected	Not Detected	Not Detected	iron ore
	Magnetite	Fe304	Well Detected	Not Detected	Not Detected	iron ore
	Goethite	FeO(OH)	Well Detected	Not Detected	Not Detected	iron ore
SULFIDES	Chromite	FeCr2O4	Not Detected	Not Detected	Not Detected	foundry,
	Galena	PbS	Not Detected	Not Detected	Not Detected	lead ore
	Pyrite	FeS2	Not Detected	Not Detected	Not Detected	chemical industry
	Bornite	Cu5FeS4	Not Detected	Not Detected	Not Detected	copper ore
SULFATES	Gypsum	CaSO4H2O	Not Detected	Well Detected	Well Detected	plaster and panels
	Anhydrite	CaSO4	Not Detected	Well Detected	Well Detected	plaster and panels
	Barite	BaSO4	Not Detected	Well Detected	Well Detected	drilling mud
CARBONATES	Calcite	CaCO3	Not Detected	Moderate	Well Detected	Portland cement
	Dolomite	CaMg(CO3)2	Not Detected	Moderate	Well Detected	Portland cement

	Quartz	SiO2	Not Detected	Not Detected	Well Detected	glass, calculators
	Talc	$Mg_3Si_4O_{10}(OH)_2$	Not Detected	Well Detected	Moderate	baby powder
	Kaolinite	$Al_4Si_4O_{10}(OH)_8$	Not Detected	Well Detected	Moderate	ceramics
SILICATES	Feldspar (orthoclase)	$(Ba,Ca,Na,K,NH_4)(Al,B,Si)_4O_8$	Not Detected	Not Detected	Well Detected	glassmaking, ceramics
	Muscovite	$KAl_2(AlSi_3O_{10})(OH,F)_2$	Not Detected	Well Detected	Moderate	paint, cement
	Chlorite	$(Fe,Mg,Al)_6(Si,Al)_4O_{10}(OH)_8$	Not Detected	Well Detected	Moderate	food industry
	Pyroxene	$XY(SiO_3)_2$	Well Detected	Moderate	Well Detected	cement production
	Limonite	$FeO(OH),nH_2O$	Well Detected	Not Detected	Not Detected	iron ore pigment
HYDROXIDES	Bauxite	$Al(OH)_3, nH_2O$	Well Detected	Not Detected	Not Detected	aluminium ore
	Jarosite	$K+Fe3+3(OH−)6(SO42−)2$	Well Detected	Not Detected	Not Detected	

An automatic method for comparing spectral curves extracted from images with spectral library curves derived from field or laboratory measurements is known as the Spectral Angle Mapper (SAM). Spectral curves from reference libraries—such as those provided by the USGS laboratory or JPL—or spectral curves derived from imagery (referred to as endmembers) can be used as reference inputs. The spectral response values of a pixel in *n* channels can be represented as vector coordinates in an *n*-dimensional space, with each spectral response forming a vector. The SAM algorithm is based on the comparison between these spectral vectors and reference spectra from known materials (Hosseinzadeh & Nowrouzi, 2024).

As a supervised classification method, the SAM algorithm has demonstrated strong efficiency in mineral mapping. By calculating the spectral angle between a pixel spectrum and a reference spectrum, SAM effectively identifies mineral classes, making it particularly suitable for detecting carbonate and silicate minerals in geologically complex terrains (Maimouni et al., 2012).

The North Region of Cameroon extends between 8° and 10° north latitude and between 12° and 16° east longitude. It is bounded to the north by the Far North Region, to the south by the Adamaoua Region, to the east by Chad and the Central African Republic, and to the west by Nigeria (Raunet, 2003).

Geologically, the literature situates the North Cameroon region within the Pan-African belt, a mobile zone that includes several domains: South Cameroon, Centre Cameroon (Adamaoua), and North Cameroon. The North Cameroon domain is of particular interest for this study because it hosts the Guider and Bossoum-Pologozom plutons, which have been the subject of investigations into their petrographic, structural, magnetic, and geochronological characteristics, as well as their broader geodynamic implications (Dawaï et al., 2022).

Research findings also highlight the mineral potential of the North Region, which is notably enriched in carbonate and silicate resources. For example, a World Bank-supported study reported the discovery of a feldspar

deposit at Bogou, located at the foot of Tinguelin Mountain, approximately 15 kilometers from the town of Garoua (Boyabe et al., 2020).

3. Methodology

3.1. Study Area

The study site is located in the North Region of Cameroon, precisely around Tinguelin Mountain at coordinates 9°26′15″N and 13°27′02″E. This area is characterized by granitoid formations and plutonic intrusions that suggest the potential presence of carbonate and silicate mineralizations. Its semi-arid climate and relatively sparse vegetation make it particularly suitable for remote sensing analysis, since the reduced canopy cover limits spectral interference. Topographically, the landscape alternates between granitic hills and plains with lateritic soils, providing diverse spectral responses (Figure 2).

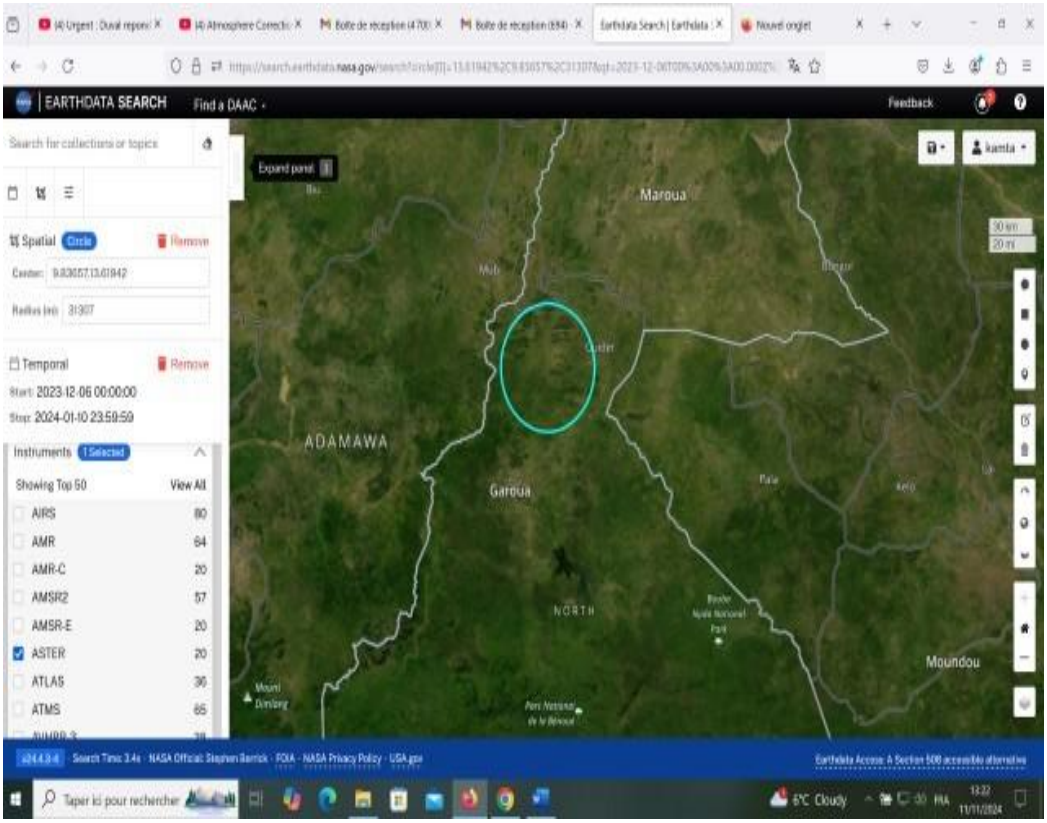

Figure 2: Geographic location of the Tinguelin Mountain study area in the North Region of Cameroon (Nasa website: earth data)

3.2. Data Acquisition and Preprocessing

Satellite imagery of the study area was acquired from NASA's TERRA platform. The dataset was imported into ENVI 5.6, where Regions of Interest (ROIs) were defined to restrict the analysis to geologically relevant areas. An atmospheric correction was then performed using the QUAC (Quick Atmospheric Correction) algorithm in order to reduce atmospheric effects and enhance spectral fidelity.

As illustrated in Figure 3, the methodological workflow consisted of a sequence of preprocessing, endmember selection, parameter setting, and mineral classification using the SAM algorithm. The ASTER image used in this study was acquired on 10 February 2023.

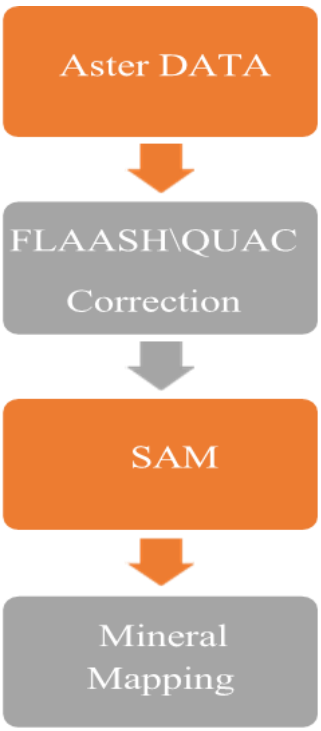

Figure3: General workflow adopted for ASTER data preprocessing and mineral classification using the SAM algorithm.

3.3. Treatment Steps

3.3. 1. Pre-processing

The ASTER image was first imported into ENVI 5.6 (Figure 4). The analysis was then restricted by defining Regions of Interest (ROIs) covering the zones with the highest geological potential (Figure 5). Radiometric and atmospheric corrections were applied to these ROIs using the QUAC algorithm, which improved the quality of the reflectance spectra and reduced distortions caused by the atmosphere (Figures 6a and 6b).

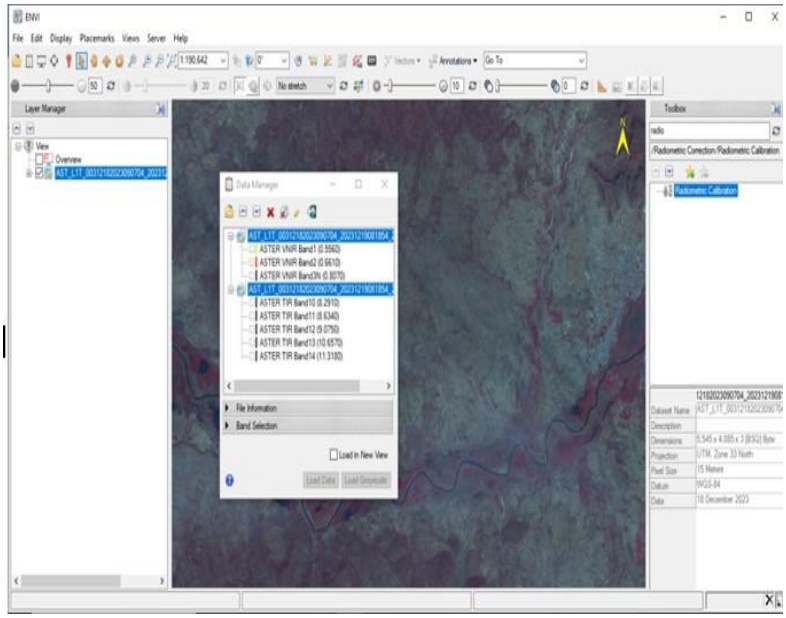

Figure 4: Importation of ASTER Level 1T image into ENVI 5.6.

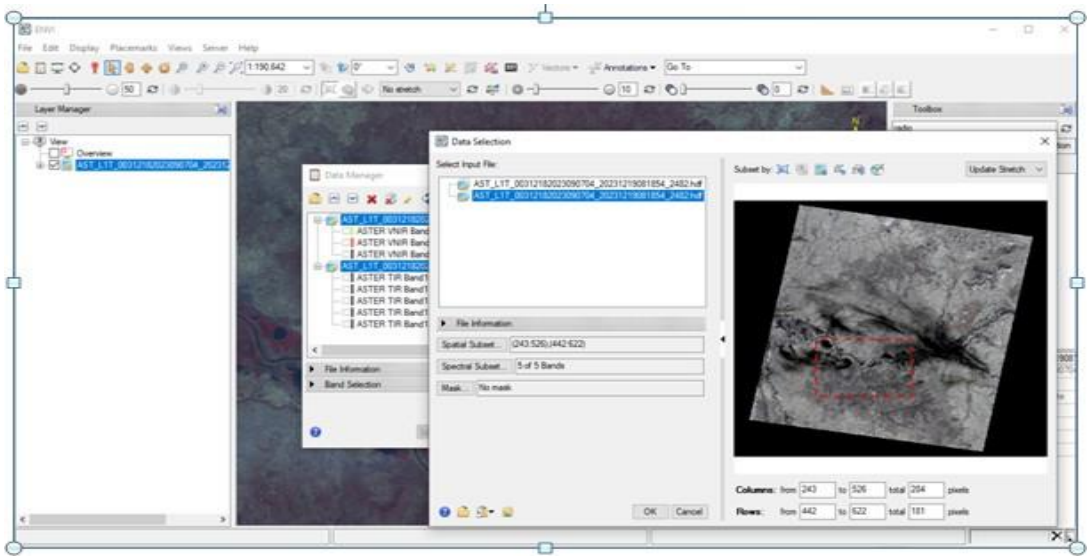

Figure 5: Definition of Regions of Interest (ROIs) within the study area.

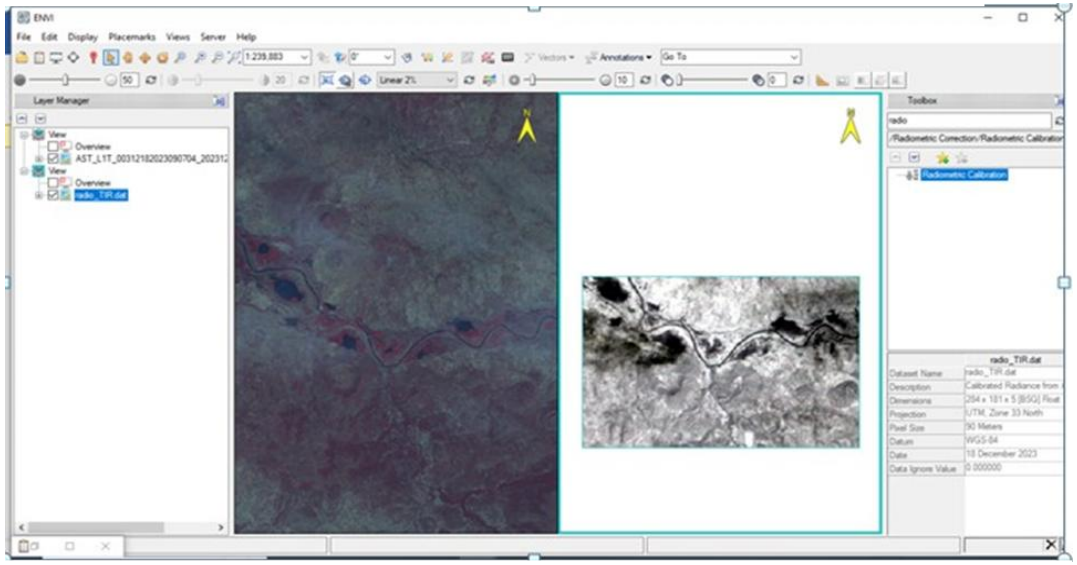

Figure 6b: Corrected spectral response of ROI1 after atmospheric adjustment.

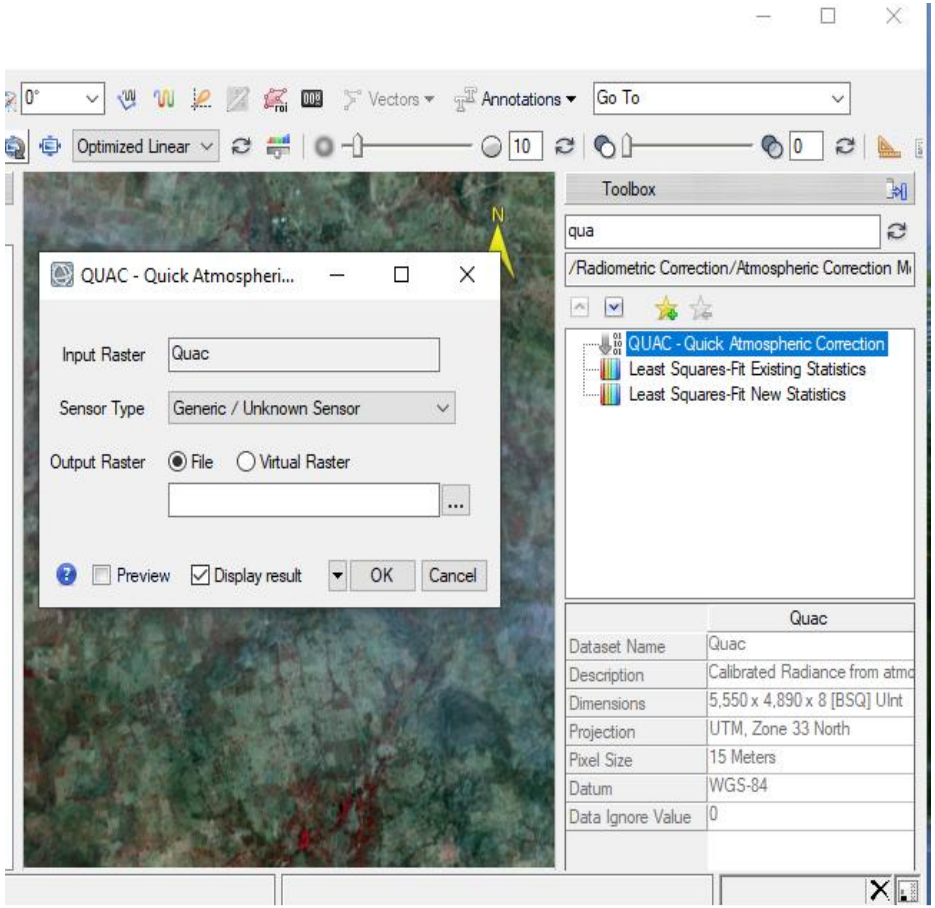

Figure 6a: Radiometric and atmospheric correction of ROI1 using the QUAC algorithm.

After preprocessing the ASTER satellite data from the selected Region of Interest (ROI), the Spectral Angle Mapper (SAM) algorithm was calibrated using spectral signatures of feldspars and calcite extracted from the ENVI spectral library. Once the algorithm was trained, the spectral information from the ROI pixels was introduced into the classification process. SAM then compared each pixel spectrum with the reference signatures from the library and assigned them to the most similar class. This procedure resulted in a mineralogical distribution map where the spatial occurrence of feldspars, calcite, and other detected minerals could be clearly distinguished.

3.3.2 . Selection of training data

The Spectral Angle Mapper (SAM) algorithm requires representative reference spectra, or endmembers, to perform mineral classification. For this purpose, spectral signatures were extracted directly from the ENVI spectral library. Feldspars, which constitute a major group of silicate minerals, were subdivided into their principal subgroups available in the library. These included plagioclases such as albite and anorthite, as well as potassium feldspars such as sanidine, orthoclase, and microcline. The selection of feldspar endmembers during the SAM configuration is shown in Figure 7.

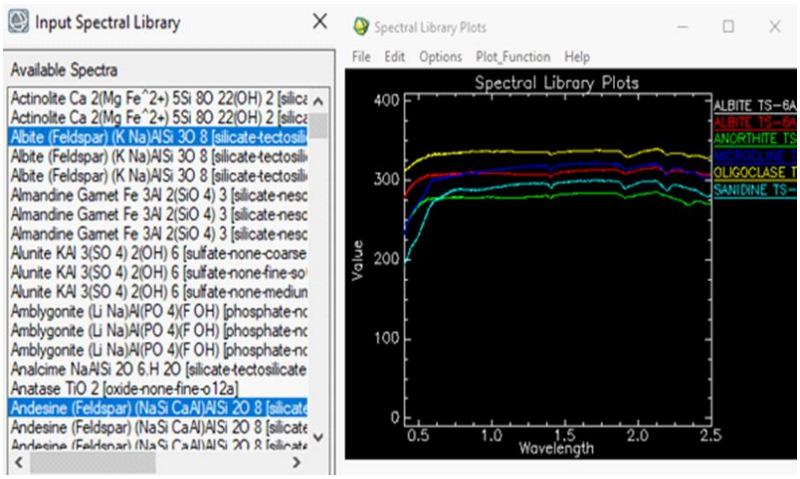

Figure 7: Selection of feldspar endmembers from the ENVI spectral library.

Similarly, carbonate minerals of particular importance in this study, such as calcite and dolomite, were also chosen as endmembers to serve as spectral references (Figure 8).

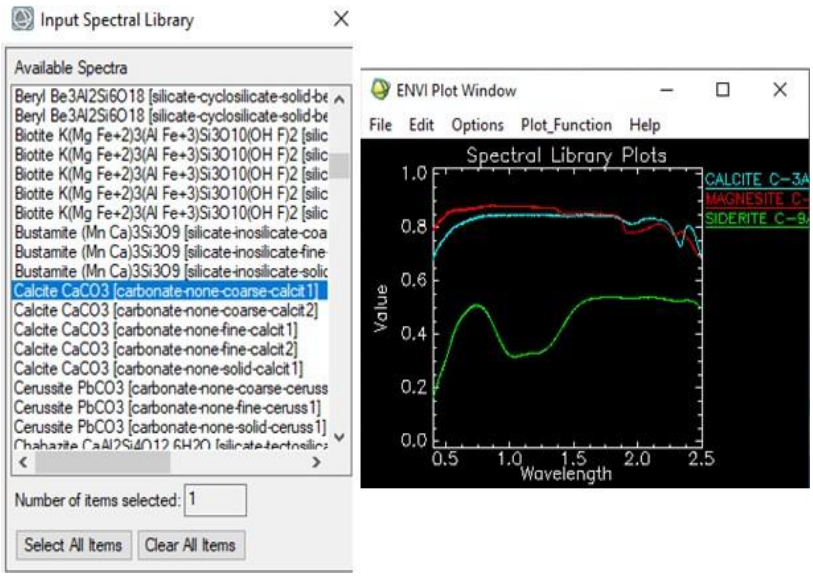

Figure 8. Selection of carbonate endmembers from the ENVI spectral library.

During the configuration of the SAM function in ENVI, windows appear allowing the user to select the reference minerals to be compared with the pixels of the Regions of Interest (ROIs). In this study, two ROIs were defined: ROI1, where feldspar signatures were analyzed, and ROI2, where carbonate signatures such as calcite were tested. These endmember selections constituted the spectral reference base for the SAM classification.

After the preprocessing of the ASTER image, the spectral information of the ROIs was introduced into the trained algorithm. The SAM routine then compared the spectral responses of each pixel in the ROIs with the chosen library signatures. Pixels were classified into the mineralogical class with the smallest spectral angle, and the resulting outputs provided a distribution map highlighting the spatial occurrence of feldspars, calcite, and other detected minerals.

Here we select the minerals we are looking for in RO2 in the ENVI spectral library. This window appears when the SAM function is executed and is therefore part of its configuration.

3.3. 3 . SAM parameters

The classification of minerals using the Spectral Angle Mapper (SAM) requires the definition of threshold parameters that determine the degree of similarity between pixel spectra and reference endmember spectra. In this study, the maximum spectral angle threshold was set to 0.1 radians. This value represents the upper limit of acceptable similarity: pixels with an angle greater than this threshold are excluded from classification to reduce errors and misidentification.

The parameter configuration was performed in ENVI 5.6 using the SAM function interface (Figure 9). The default option of a single threshold value was maintained, ensuring a consistent classification rule across all Regions of Interest (ROIs). By adopting this parameter, only pixels exhibiting strong spectral fidelity to feldspar and carbonate signatures from the library were retained in the final mineralogical maps.

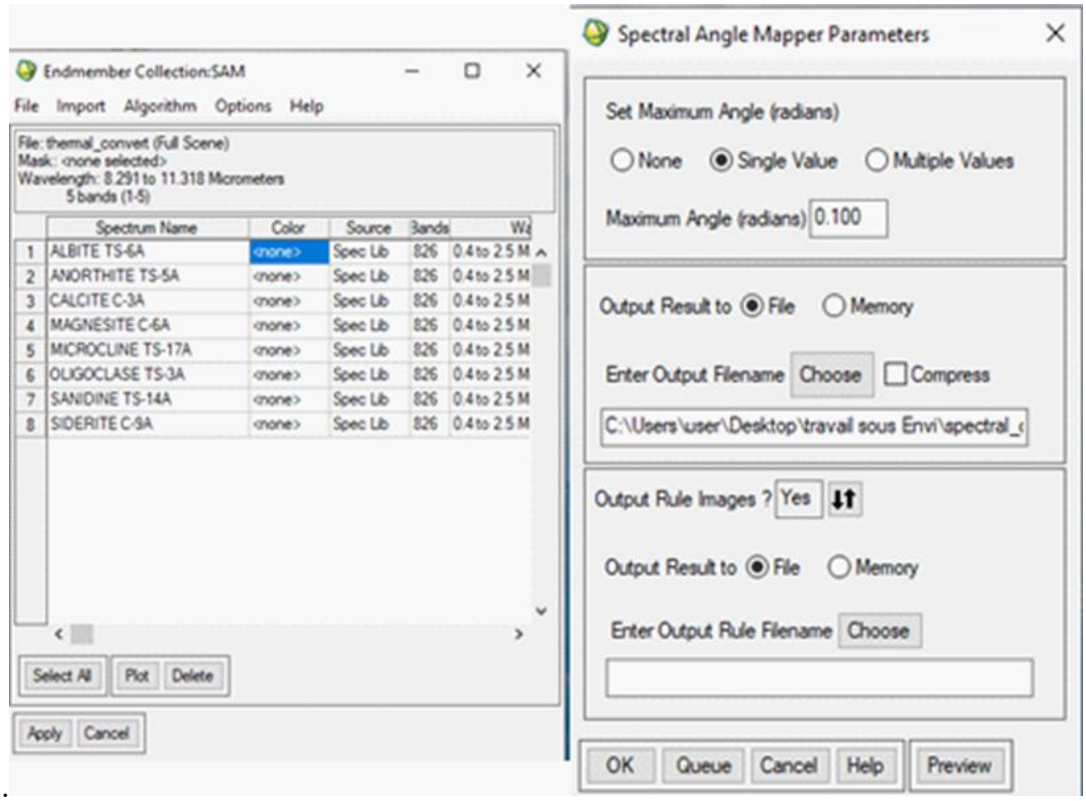

Figure 9: Configuration of SAM classification parameters with a 0.1 radian maximum threshold**.**

This step is crucial because the spectral variability of minerals in satellite imagery can be influenced by factors such as illumination conditions, surface weathering, and pixel mixing. The use of a strict threshold therefore helped to increase the reliability of the mineral detection results, while minimizing false positives.

4. Results

Two Regions of Interest (ROIs) were analyzed after applying the Spectral Angle Mapper (SAM) classification. The outputs highlight the spatial distribution of feldspars, calcite, and other minerals within the study area.

ROI1

In the first Region of Interest (ROI1), the SAM algorithm successfully detected albite, a representative member of the plagioclase feldspar group. Albite was mapped in red and white tones depending on the classification window, covering approximately 15% of the ROI. In addition to albite, a significant proportion of magnetite was identified, represented by purple areas, which occupied nearly 45% of the ROI. Although magnetite was not the primary target of this study, its strong spectral response was clearly detected by the algorithm, confirming the robustness of the classification (Figures 10).

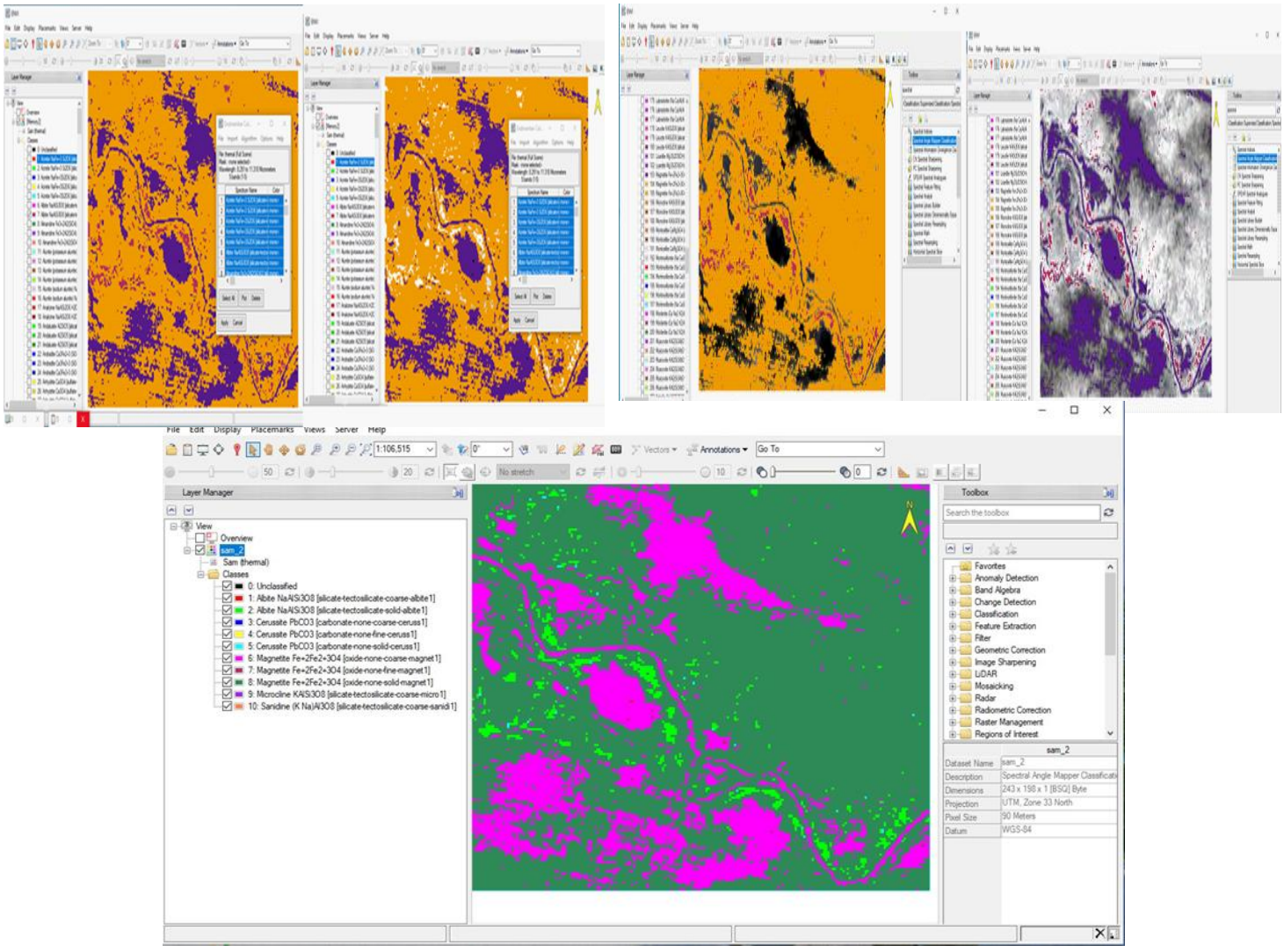

Figure 10: SAM classification results for ROI1 showing the distribution of albite (≈15%) and magnetite (≈45%).

The mineralogical characterization of ROI1 therefore confirmed the presence of albite, consistent with the geological context of the region, while also revealing magnetite as an additional component. This finding

illustrates the capacity of SAM to identify minerals beyond the predefined targets when their spectral features are sufficiently distinctive.

ROI2

In the second Region of Interest (ROI2), the SAM algorithm confirmed the presence of calcite. Depending on the visualization parameters in ENVI, calcite appeared in black or yellow, corresponding to whether the mineral was actively selected or deselected in the classification window. Approximately 20% of the ROI was classified as calcite, providing strong evidence of carbonate mineralization within this part of the study area (Figure 11).

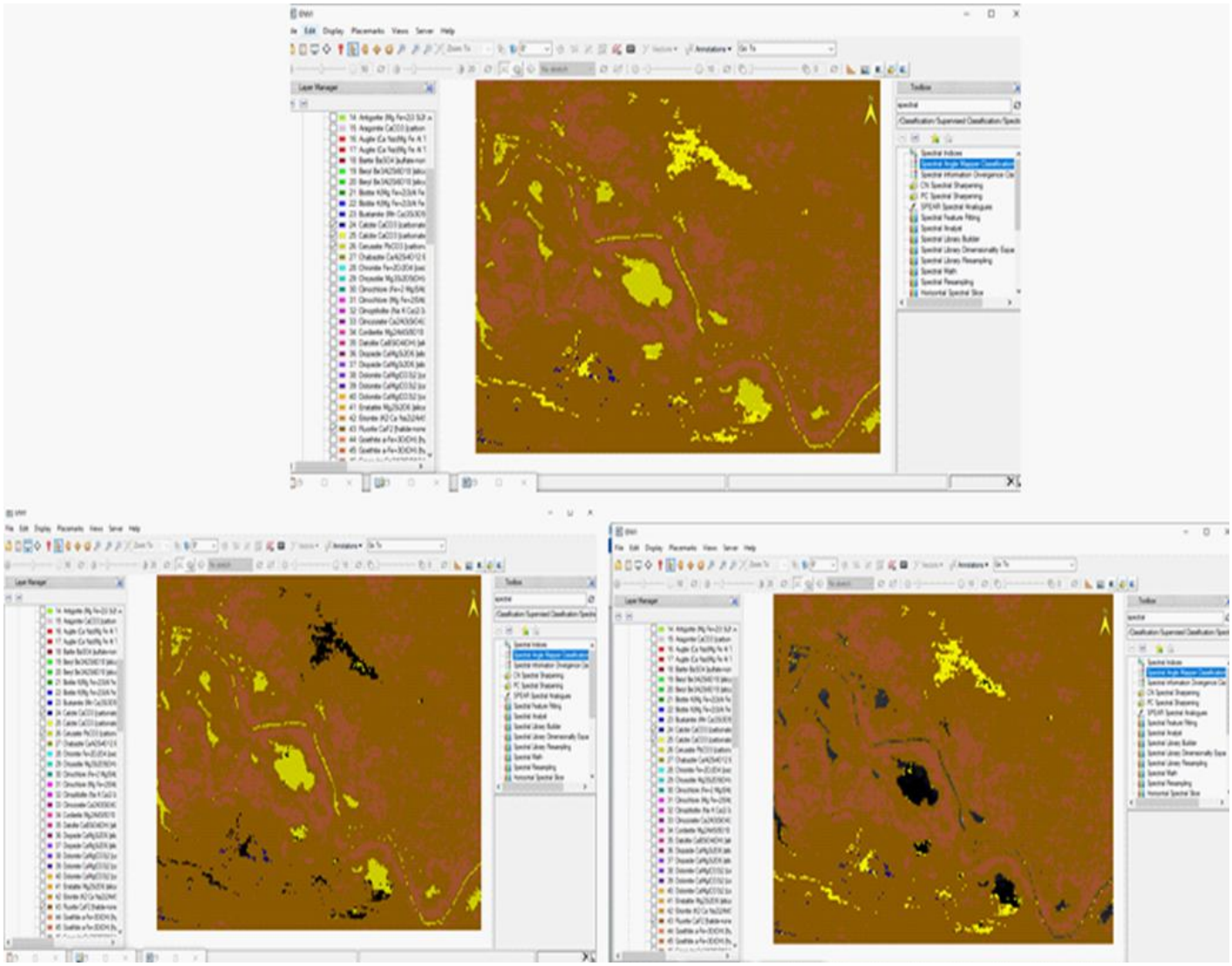

Figure 11: SAM classification results for ROI2 indicating the presence of calcite (≈20%).

Accuracy and Reliability of SAM Results

To evaluate the performance of the supervised SAM classification, a confusion matrix was generated (Figure 12). This matrix compared the classified pixel values with the corresponding reference spectra, thereby providing a quantitative measure of classification reliability.

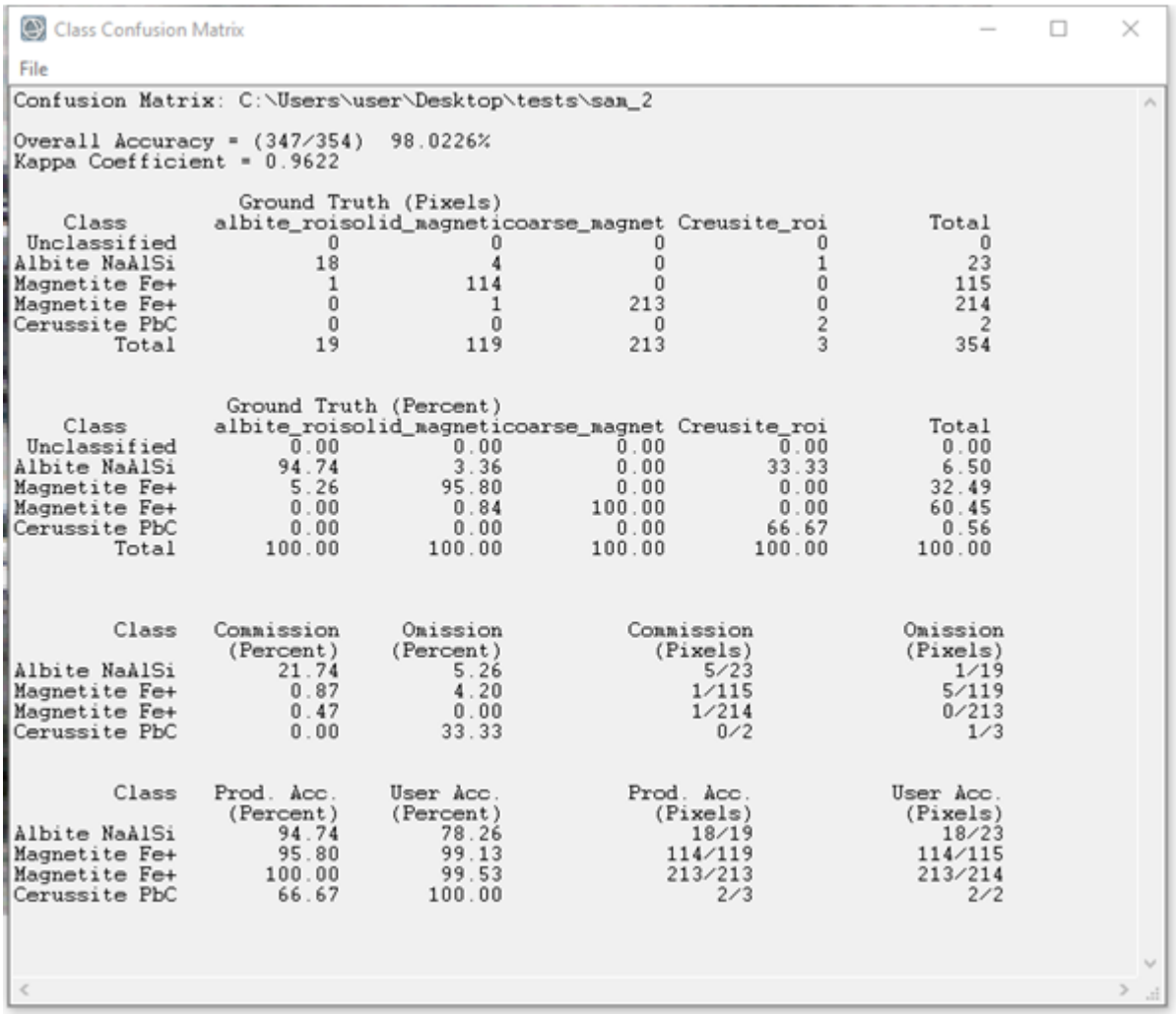

Class Confusion Matrix

File

Confusion Matrix: C:\Users\user\Desktop\tests\sam_2

Overall Accuracy = (347/354) 98.0226%
Kappa Coefficient = 0.9622

Ground Truth (Pixels)

Class	albite_roi	solid_magnetic	coarse_magnet	Creusite_roi	Total
Unclassified	0	0	0	0	0
Albite NaAlSi	18	4	0	1	23
Magnetite Fe+	1	114	0	0	115
Magnetite Fe+	0	1	213	0	214
Cerussite PbC	0	0	0	2	2
Total	19	119	213	3	354

Ground Truth (Percent)

Class	albite_roi	solid_magnetic	coarse_magnet	Creusite_roi	Total
Unclassified	0.00	0.00	0.00	0.00	0.00
Albite NaAlSi	94.74	3.36	0.00	33.33	6.50
Magnetite Fe+	5.26	95.80	0.00	0.00	32.49
Magnetite Fe+	0.00	0.84	100.00	0.00	60.45
Cerussite PbC	0.00	0.00	0.00	66.67	0.56
Total	100.00	100.00	100.00	100.00	100.00

Class	Commission (Percent)	Omission (Percent)	Commission (Pixels)	Omission (Pixels)
Albite NaAlSi	21.74	5.26	5/23	1/19
Magnetite Fe+	0.87	4.20	1/115	5/119
Magnetite Fe+	0.47	0.00	1/214	0/213
Cerussite PbC	0.00	33.33	0/2	1/3

Class	Prod. Acc. (Percent)	User Acc. (Percent)	Prod. Acc. (Pixels)	User Acc. (Pixels)
Albite NaAlSi	94.74	78.26	18/19	18/23
Magnetite Fe+	95.80	99.13	114/119	114/115
Magnetite Fe+	100.00	99.53	213/213	213/214
Cerussite PbC	66.67	100.00	2/3	2/2

Figure 12: Confusion matrix of the SAM classification results.

As shown in the confusion matrix, the Kappa coefficient obtained was between 0.8 and 1.0. This high value indicates a strong agreement between the classification outputs and the reference data, confirming that the SAM algorithm achieved a sufficiently precise and reliable discrimination of mineral classes within the study area.

5. Discussion

The combination of ASTER satellite data and the Spectral Angle Mapper (SAM) algorithm proved to be an effective approach for the detection and mapping of carbonate and silicate minerals in the northern region of Cameroon. The results obtained in ROI1 demonstrated the presence of albite, a plagioclase feldspar, and magnetite, while ROI2 confirmed the occurrence of calcite. These findings highlight the potential of supervised spectral classification to identify key minerals relevant for both academic research and industrial applications.

The detection of albite and calcite is consistent with the geological setting of the region, which is characterized by granitoid intrusions and carbonate-bearing lithologies. The identification of magnetite, although not initially targeted, illustrates the sensitivity of SAM to strong spectral features and confirms its usefulness for broader mineralogical surveys. This outcome supports previous studies that have demonstrated the suitability of SAM for mineral exploration, particularly for carbonate and feldspar-rich environments (Zhang & Li, 2014; Sudharsan et al., 2019b; Bishop et al., 2011).

One of the main advantages of the SAM algorithm lies in its relative insensitivity to illumination conditions, making it suitable for regions such as northern Cameroon where varying topography and seasonal effects can complicate spectral analysis. However, the method is not without limitations. The low spectral resolution of

ASTER compared to hyperspectral sensors reduces its ability to discriminate between minerals with very similar spectral signatures. For instance, other feldspars present in the spectral library were not clearly distinguished in the classification results. Mixed pixels within ASTER imagery also contributed to the omission of certain mineral classes.

These limitations suggest that while SAM combined with ASTER data is efficient for a first-level exploration, more advanced approaches could further enhance mineral discrimination. Unsupervised deep learning methods, particularly Convolutional Neural Networks (CNNs), offer opportunities to integrate both spectral and spatial information for improved classification. Likewise, the use of hyperspectral datasets such as those provided by the Hyperion sensor aboard the Earth Observer-1 (EO-1) satellite—with its 222 narrow bands—would significantly improve spectral discrimination. Such developments could complement the findings of this study by refining the detection of feldspar subgroups and carbonate variations in future research.

Overall, the discussion highlights that the methodology applied here validates earlier findings in the literature while also pointing to the potential of emerging artificial intelligence techniques in geological remote sensing. In the specific context of Cameroon, where traditional field exploration remains costly and time-consuming, the approach provides a valuable alternative for identifying promising mineral targets and guiding future ground surveys.

6. Conclusion

Remote sensing has proven to be a powerful and cost-effective tool for mineral exploration in regions such as northern Cameroon, where accessibility challenges and limited infrastructure make traditional field surveys time-consuming and expensive. By integrating ASTER multispectral data with the supervised Spectral Angle Mapper (SAM) algorithm in ENVI 5.6, this study demonstrated the reliable identification of carbonate and silicate minerals, particularly albite and calcite, within underexplored areas of the North Region.

The results contribute to improving knowledge of the mineral potential of Cameroon and provide valuable insights for the enhancement of the national Geographic and Mining Information System (GMIS). Beyond confirming the presence of minerals consistent with the geological setting, the study highlights the practical advantages of remote sensing techniques for preliminary exploration campaigns. The ability to map mineral distribution at relatively low cost represents a strategic advantage for developing countries, where resources for extensive field exploration are often limited.

At the same time, this research underlines the inherent limitations of ASTER data. The relatively coarse spectral resolution restricted the discrimination of certain feldspar subgroups and limited the identification of minerals with overlapping spectral features. To address these challenges, future studies should consider the use of hyperspectral datasets, such as those provided by the Hyperion sensor aboard Earth Observer-1, which offers much finer spectral detail. Likewise, the adoption of advanced classification approaches, including deep learning methods such as Convolutional Neural Networks (CNNs), could further improve the robustness of mineral mapping by incorporating both spectral and spatial information.

The scientific contribution of this work lies not only in validating the effectiveness of SAM with ASTER imagery for mineral detection but also in opening pathways toward more sophisticated techniques. By combining remote sensing technologies with artificial intelligence, future research can strengthen the reliability of mineral exploration and support sustainable resource management in Cameroon.

Financial supports

No funds, grants or other financial support was received to conduct this study or to prepare the manuscript.

Competing interests

The authors declare that they have no known competing financial interests or personal relationships that could have appeared to influence the work reported in this paper.

Acknowledgements.

The authors would like to express their sincere gratitude to the supervisory team of the LGISDIA Laboratory at the National Polytechnic School of Douala for their valuable guidance and constructive advice throughout this research.

References

1. Aquilano, D., Otálora, F., Pastero, L., & García-Ruiz, J. M. (2016). Three study cases of growth morphology in minerals: Halite, calcite and gypsum. *Progress in Crystal Growth and Characterization of Materials, 62*(2), 227–251. https://doi.org/10.1016/j.pcrysgrow.2016.04.012
2. Bell, A., del-Blanco, C. R., Jaureguizar, F., Jurado, M. J., & García, N. (2022). Automatic mineral recognition in hyperspectral images using a semantic-segmentation-based deep neural network trained on a hyperspectral drill-core database. *SSRN Electronic Journal.* https://doi.org/10.2139/ssrn.4090740
3. Bernstein, L. S., Adler-Golden, S. M., Sundberg, R. L., Levine, R. Y., Perkins, T. C., Berk, A., Ratkowski, A. J., Felde, G., & Hoke, M. L. (2005). Validation of the QUick atmospheric correction (QUAC) algorithm for VNIR-SWIR multi- and hyperspectral imagery. In S. S. Shen & P. E. Lewis (Eds.), *Proceedings of SPIE* (p. 668). https://doi.org/10.1117/12.603359
4. Bishop, C. A., Liu, J. G., & Mason, P. J. (2011). Hyperspectral remote sensing for mineral exploration in Pulang, Yunnan Province, China. *International Journal of Remote Sensing, 32*(9), 2409–2426. https://doi.org/10.1080/01431161003698336
5. Boardman, J. W. (1993). Automating spectral unmixing of AVIRIS data using convex geometry concepts. In *Summaries of the 4th Annual JPL Airborne Geoscience Workshop, Volume 1: AVIRIS Workshop* (pp. 11–14). JPL.
6. Boyabe, M., Dawai, D., Tchameni, R., & Tchunte, P. M. F. (2020). Petrography and mineralogy of the quartz and quartz-feldspar sulphide veins in the Pan-African syenitic massif of Guider (North Cameroon). *Open Journal of Geology, 10*(3), 235–259. https://doi.org/10.4236/ojg.2020.103013
7. Dawaï, D., Saha Fouotsa, A. N., Bello, A., Tchameni, R., Nédélec, A., & Bouchez, J.-L. (2022). Petrology of the late Pan-African Guider syenite pluton (Cameroon): Implications for magma genesis and emplacement. *Journal of African Earth Sciences, 190*, 104519. https://doi.org/10.1016/j.jafrearsci.2022.104519
8. Fauvel, M., Tarabalka, Y., Benediktsson, J. A., Chanussot, J., & Tilton, J. C. (2012). Advances in spectral-spatial classification of hyperspectral images. *Proceedings of the IEEE, 101*(3), 652–675. https://doi.org/10.1109/JPROC.2012.2197150
9. Hosseinzadeh, H., & Nowrouzi, G. (2024). Application of SAM and MTMF methods in differentiating hydrothermal alterations related to metallic mineralization potential, Nignan exploration area. *Journal of Geomine, 2*(2), 102–120.
10. Islam, N. U., Zhang, Q., Qiu, W., Liu, L., Khalil, Y. S., Ahmad, S. M., & Ahmad, W. (2024). Mineralogical mapping and lithological discrimination by using ASTER remote sensing data in the Chitral region, Khyber Pakhtunkhwa, Northern Pakistan. *Earth Science Informatics, 17*(6), 6075–6094. https://doi.org/10.1007/s12145-024-01483-4
11. Kruse, F. A., Lefkoff, A. B., Boardman, J. W., Heidebrecht, K. B., Shapiro, A. T., Barloon, P. J., & Goetz, A. F. (1993). The spectral image processing system (SIPS): Interactive visualization and analysis of imaging spectrometer data. *Remote Sensing of Environment, 44*(2–3), 145–163. https://doi.org/10.1016/0034-4257(93)90013-N
12. Kyonka, J. C., & Cook, R. L. V. (1954). The properties of feldspars and their use in whitewares. *Bulletin, University of Illinois Engineering Experiment Station*, No. 422.
13. Li, J., Bioucas-Dias, J. M., & Plaza, A. (2012). Semisupervised hyperspectral image classification using soft sparse multinomial logistic regression. *IEEE Geoscience and Remote Sensing Letters, 10*(2), 318–322. https://doi.org/10.1109/LGRS.2012.2200478
14. Maimouni, S., Bannari, A., El-Harti, A., & El-Ghmari, A. (2012). Indices spectraux et "Spectral Angle Mapper" pour la cartographie des risques d'érosion hydrique à partir des données ALI EO-1. *Revue Marocaine des Sciences Agronomiques et Vétérinaires, 10*(4), 47–55.
15. Mezned, N., Fatnassi, A., & Abdeljaouad, S. (2019). Application of ASTER multispectral data and hyperspectral spectroscopy for phosphate exploration. In C. Mueller, W. Assibey-Bonsu, E. Baafi, C. Dauber, C. Doran, M. J. Jaszczuk, & O. Nagovitsyn (Eds.), *Mining goes digital* (pp. 86–93). CRC Press. https://doi.org/10.1201/9780429320774-10
16. Ousmanou, S., Martial, F. E., Jules, T. K., Ludovic, A. M., Agnès Blandine, K. T., Sufinatu, A., Mohamed, R., & Maurice, K. (2024). Mapping and discrimination of the mineralization potential in granitoids from Banyo area (Adamawa, Cameroon) using Landsat 9 OLI, ASTER images and field observations. *Geosystems and Geoenvironment, 3*(1), 100239. https://doi.org/10.1016/j.geogeo.2023.100239

17. Peyghambari, S., & Zhang, Y. (2021). Hyperspectral remote sensing in lithological mapping, mineral exploration, and environmental geology: An updated review. *Journal of Applied Remote Sensing*, *15*(3), 031501. https://doi.org/10.1117/1.JRS.15.031501
18. Plaza, A., Benediktsson, J. A., Boardman, J. W., Brazile, J., Bruzzone, L., Camps-Valls, G., Chanussot, J., Fauvel, M., Gamba, P., & Gualtieri, A. (2009). Recent advances in techniques for hyperspectral image processing. *Remote Sensing of Environment*, *113*, S110–S122. https://doi.org/10.1016/j.rse.2007.07.028
19. Qi, J., Inoue, Y., & Wiangwang, N. (2018). Hyperspectral remote sensing in global change studies. In *Fundamentals, sensor systems, spectral libraries, and data mining for vegetation* (pp. 55–77). CRC Press. https://doi.org/10.1201/9781315164151-3
20. Rajendran, S., & Nasir, S. (2017). Characterization of ASTER spectral bands for mapping of alteration zones of volcanogenic massive sulphide deposits. *Ore Geology Reviews*, *88*, 317–335. https://doi.org/10.1016/j.oregeorev.2017.04.025
21. Raunet, M. (2003). Quelques clés morphopédologiques pour le Nord Cameroun à l'usage des agronomes. *Cahiers Agricultures*, *12*(3), 161–170.
22. Son, Y.-S., Lee, G., Lee, B. H., Kim, N., Koh, S.-M., Kim, K.-E., & Cho, S.-J. (2022). Application of ASTER data for differentiating carbonate minerals and evaluating MgO content of magnesite in the Jiao-Liao-Ji Belt, North China Craton. *Remote Sensing*, *14*(1), 181. https://doi.org/10.3390/rs14010181
23. Sudharsan, S., Hemalatha, R., & Radha, S. (2019a). A survey on hyperspectral imaging for mineral exploration using machine learning algorithms. In *2019 International Conference on Wireless Communications, Signal Processing and Networking (WiSPNET)* (pp. 206–212). IEEE. https://doi.org/10.1109/WiSPNET45539.2019.9032740
24. Sudharsan, S., Hemalatha, R., & Radha, S. (2019b). A survey on hyperspectral imaging for mineral exploration using machine learning algorithms. In *2019 International Conference on Wireless Communications, Signal Processing and Networking (WiSPNET)* (pp. 206–212). IEEE. https://doi.org/10.1109/WiSPNET45539.2019.9032740
25. Yokoya, N., Chan, J. C.-W., & Segl, K. (2016). Potential of resolution-enhanced hyperspectral data for mineral mapping using simulated EnMAP and Sentinel-2 images. *Remote Sensing*, *8*(3), 172. https://doi.org/10.3390/rs8030172
26. Zeng, H., Han, X., & Liu, Q. (2021). Mineral detection from hyperspectral images using a spatial-spectral residual convolution neural network. *Journal of Physics: Conference Series*, *1894*(1), 012104. https://doi.org/10.1088/1742-6596/1894/1/012104
27. Zhang, X., & Li, P. (2014). Lithological mapping from hyperspectral data by improved use of spectral angle mapper. *International Journal of Applied Earth Observation and Geoinformation*, *31*, 95–109. https://doi.org/10.1016/j.jag.2014.03.007